Eruption of the EUV Hot Channel from the Solar Limb and Associated Moving Type IV Radio Burst

P. Vemareddy[1] , P. Démoulin[2,3] , K. Sasikumar Raja[1] , J. Zhang[4] , N. Gopalswamy[5] , and N. Vasantharaju[1]
[1] Indian Institute of Astrophysics, II Block, Koramangala, Bengaluru-560 034, India; vemareddy@iiap.res.in
[2] LESIA, Observatoire de Paris, Université PSL, CNRS, Sorbonne Université, Université de Paris, 5 place Jules Janssen, F-92190 Meudon, France
[3] Laboratoire Cogitamus, rue Descartes, F-75005 Paris, France
[4] Department of Physics and Astronomy, George Mason University, Fairfax, VA 22030, USA
[5] Goddard Space Flight Center, Greenbelt, MD 20771, USA

Abstract

Using the observations from the Solar Dynamics Observatory, we study an eruption of a hot-channel flux rope (FR) near the solar limb on 2015 February 9. The pre-eruptive structure is visible mainly in EUV 131 Å images, with two highly sheared loop structures. They undergo a slow rising motion and then reconnect to form an eruptive hot channel, as in the tether-cutting reconnection model. The J-shaped flare ribbons trace the footpoint of the FR that is identified as the hot channel. Initially, the hot channel is observed to rise slowly at 40 km s^{-1}, followed by an exponential rise from 22:55 UT at a coronal height of 87 ± 2 Mm. Following the onset of the eruption at 23:00 UT, the flare reconnection then adds to the acceleration process of the coronal mass ejection (CME) within $3 R_\odot$. Later on, the CME continues to accelerate at 8 m s^{-2} during its propagation period. Further, the eruption also launched type II radio bursts, which were followed by type III and type IVm radio bursts. The start and end times of the type IVm burst correspond to the CME's core height of 1.5 and 6.1 $R_\odot$, respectively. Also, the spectral index is negative, suggesting that nonthermal electrons are trapped in the closed loop structure. Accompanied by this type IVm burst, this event is unique in the sense that the flare ribbons are very clearly observed together with the erupting hot channel, which strongly suggests that the hooked parts of the J-shaped flare ribbons outline the boundary of the erupting FR.

Unified Astronomy Thesaurus concepts: Solar radio emission (1522); Solar prominences (1519); Solar coronal mass ejections (310); Solar magnetic reconnection (1504)

Supporting material: animation

1. Introduction

Magnetic reconnection is a fundamental physical process that has a prime role, especially in releasing magnetic energy during solar eruptions (e.g., Priest & Forbes 2000; Pontin 2012). When a magnetic configuration has an excess of magnetic energy, a trigger is required to initiate the eruption. Several physics-based models have been invoked to explain the onset mechanism of an eruption. Of these, the tether-cutting or flux cancellation model (van Ballegooijen & Martens 1989; Moore et al. 2001) and the magnetic breakout model (Antiochos et al. 1999) come under the category of reconnection-based models. In these models, the initial sheared core field along the magnetic polarity inversion line (PIL) is enveloped by the overlying potential arcade, and the reconnection either in the inner arcade or in the overlying field triggers the eruption. Other models rely on an ideal MHD instability, viz., kink and torus instabilities, with the presumption that the pre-eruptive structure is a twisted magnetic flux rope (FR; Forbes & Isenberg 1991; Török & Kliem 2005; Forbes et al. 2006; Kliem & Török 2006). The destabilization is realized when either a critical twist or a too-steeply-decreasing background field is reached. Although the mechanism triggering an eruption is different in the above models, magnetic reconnection induced underneath the uplifting FR plays an important

role during the eruption, since it allows the FR's successful ejection into the heliosphere by transforming the stabilizing upper arcade into the twisted field surrounding the original erupting core field (Lin & Forbes 2000; Aulanier et al. 2010; Welsch 2018). The resulting enlarged FR is typically observed as a coronal mass ejection (CME) and the remaining reconnected field below as postflare arcades rooted in flare ribbons.

The high-resolution space-based observations from the Transition Region and Coronal Explorer (Handy et al. 1999) and the Atmospheric Imaging Assembly (AIA; Lemen et al. 2012) on board the Solar Dynamics Observatory (SDO; Pesnell et al. 2012) provide key observations for understanding the initiation mechanism. Hα filaments, prominences, and X-ray sigmoids are also precursor features of an eruption. These features have been interpreted in the same physical framework with the presence of an FR or, alternatively, a sheared magnetic arcade (e.g., Gibson et al. 2006; Green et al. 2011; Vemareddy & Zhang 2014). Recent studies have discovered that the FR configurations prevail with hot coronal conditions of several-million-degree kelvin temperatures visible in the EUV hot channels (Zhang et al. 2012; Cheng et al. 2013).

The tether-cutting reconnection (Moore et al. 2001; Moore & Sterling 2006) was found to play both a formation and a triggering role. During the eruption, it evolves to the runaway tether-cutting reconnection below the sheared arcade, before the eruption of the core field finally occurs and a CME is launched (Yurchyshyn et al. 2006; Liu et al. 2010; Vemareddy et al. 2012). Following the onset of this eruption, a reconnection in the

overarching loop structure is mostly identified as a remote brightening. The trigger could also be due to the dynamics of the overarching loops with exceeding helical twist, as suggested by the EUV observations of the sigmoidal structure (Vemareddy & Zhang 2014).

Several observational reports have indicated that magnetic cancellation at the photospheric level induces tether-cutting reconnection between two sets of highly sheared magnetic arcades in the hours before eruption. This implies the formation of an FR that later erupts (Green et al. 2011; Vemareddy et al. 2017; Xue et al. 2017). Further, the reconnecting sheared arcades are sometimes identified as two lobes of a sigmoid. Using high-resolution Interface Region Imaging Spectrometer observations, Chen et al. (2016) reported that the tether-cutting reconnection occurs between the sheared magnetic configurations of two filaments. This leads to a flare-associated CME. The tether-cutting reconnection may also be responsible for the trigger of the CME eruption in the complex double-decker filament channel. The involved magnetic configuration was proposed to be either a double FR configuration or a single FR on top of the sheared arcades (Liu et al. 2012; Vemareddy et al. 2012; Joshi et al. 2020).

In this article, we report a unique observation of the eruption of a hot-channel FR located near the solar limb. These observations have different projection effects than similar events observed on the solar disk. This allows us to differentiate the coronal structures involved, which is crucial for understanding the triggering mechanisms of the eruptions (Chen et al. 2016; Vemareddy et al. 2017). In addition, this eruption triggers radio bursts of types III, II, and IV. Flare reconnection converts some of the magnetic energy to accelerate electrons along magnetic field lines. These fast-moving electrons set up plasma oscillations (called Langmuir waves) in the solar corona during their passage, and their subsequent conversion into electromagnetic waves produces radio emission as type III bursts (Ginzburg & Zhelezniakov 1958; Zheleznyakov & Zaitsev 1970; Melrose 1980; Sasikumar Raja & Ramesh 2013; Singh et al. 2019; Ndacyayisenga et al. 2021). Type II bursts are slow-drifting bursts (≈ 1000 km s^{-1}) generated by nonthermal electrons accelerated at shocks that propagate through the solar corona and interplanetary medium (Payne-Scott et al. 1947; Nelson & Melrose 1985, pp. 333–35; Nindos et al. 2008; Cho et al. 2013). Moving type IV radio bursts (Stewart et al. 1982; Leblanc et al. 2000; Sasikumar Raja et al. 2014) are generally believed to be produced by electrons trapped within the erupting closed structures, which have proposed as being the radio signatures of the hot-channel FRs, as evidenced by radio imaging observations (Démoulin et al. 2012; Wu et al. 2016; Vasanth et al. 2016).

We describe the EUV and magnetic observational data of the erupting hot channel in Section 2. Then, in Section 3, we first analyze the onset of the eruption; we next study the kinematics of the eruption up to 30 $R_\odot$ to constrain the physical mechanisms involved; and finally we explore the link between the radio bursts and the eruption. A summarized discussion is then given in Section 4.

2. Overview of the Observations

The studied eruption event is well captured in the EUV observations of AIA/SDO and the white-light images from the Large Angle and Spectrometric Coronagraph (LASCO;

Brueckner et al. 1995) on board the Solar and Heliospheric Observatory (SOHO). The eruption originated from active region (AR) 12282 on 2015 February 9. The AR was located near the eastern limb (N15°E60°), so it is easy to study the connection between the CME manifestation in the LASCO field of view (FOV) and the eruption features on the disk (Figure 1).

The eruption was initiated at 22:42 UT on 2015 February 9, with two loop structures (in the form of flux threads) crossing each other in projection on one side (shown at 22:52 UT in Figure 2(d)). After 22:55 UT, a single loop structure rises during the early phase of the eruption observed in AIA 131 Å (Figures 1(a) and 2(d)). This structure appears diffuse in the AIA 131 and 94 Å channels, while it is not present in the other AIA passbands (Figures 2(a)–(c)). Therefore, this erupting feature is a hot channel, as observed in other events (e.g., Zhang et al. 2012). From the AIA 193 Å observations (Figure 1), the plasma loop morphology reveals the envelope field extended up to 1.3 $R_\odot$.

The magnetic origins of this erupting feature are disclosed by the line-of-sight (LOS) magnetic field observations obtained from the Helioseismic Magnetic Imager (HMI; Schou et al. 2012) on board SDO. The AR belongs to the β-class, with a quadrupolar magnetic configuration having two sunspots of negative polarity and a following dispersed positive polarity (Figure 4). The PIL of the western bipole is with a strongly sheared field.

The subsequent rising motion of the erupting feature manifests as a CME, which first enters into the C2 FOV at 23:24 UT on February 9 and the C3 FOV at 00:06 UT on February 10. Representative images of the CME are displayed in the bottom panels of Figure 1. The three-part structures of the CME, i.e., the leading edge, dark cavity, and bright core, are well observed in the C2 images (Illing & Hundhausen 1985; Vourlidas et al. 2013, 2020). These observations are typically interpreted with the presence of an FR with/without a filament/prominence embedded in its core. However, the presence of the core may not always require an eruptive filament/prominence (Howard et al. 2017), given the projection effects. As such, the plane-of-sky-oriented FR in the AIA images is not resolvable in the coronagraph images, although they provide an impression of the rotated FR in the core of the CME. After 01:42 UT on February 10, the white-light intensity reduces, such that the CME appears as a diffused structure.

This CME is accompanied by a GOES X-ray M2.4 class flare and type II, III, and IV radio bursts. We use the observations of the Learmonth radio spectrograph located at North West Cape, Western Australia (Lobzin et al. 2010), and the Wind/Waves instrument from Lagrangian point L1 (Bougeret et al. 1995). The former instrument operates in the frequency range of 25–180 MHz, and the latter observes between 20 KHz and 14 MHz.

3. Results

3.1. Initiation of the Eruption: Observations

The erupting feature is more visible in the 131 Å passband compared to the 94 Å passband. The other channels exhibit no signatures of the erupting feature. The initiation is noticed with a loop system, L1, which appears as a small arc at 22:42 UT in 131 Å, which is later accompanied by a second loop, L2 (defined in Figure 2(d)). The loops have one of their legs
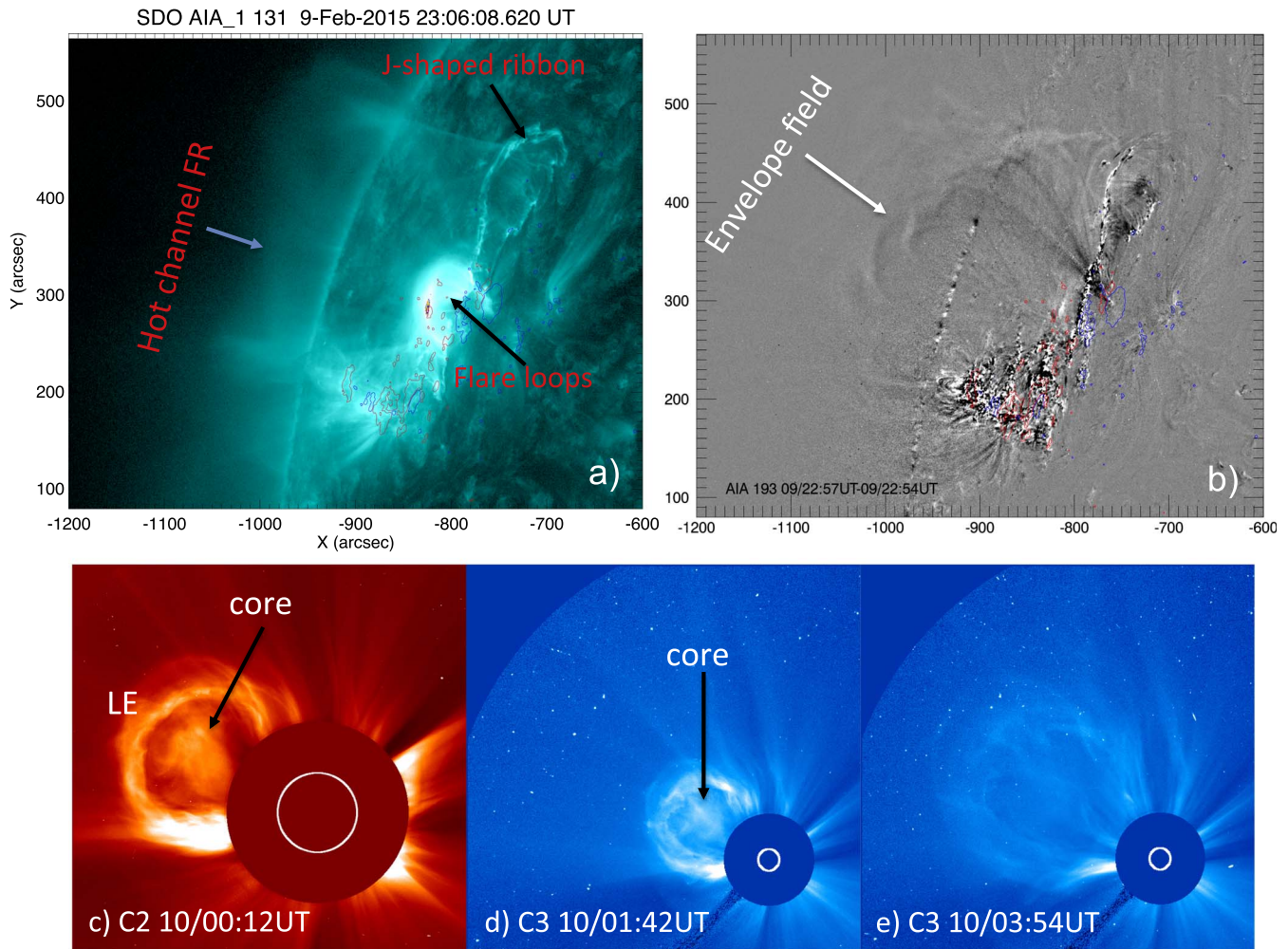
Figure 1. The hot-channel eruption from the near limb of AR 12282. Panels (a) and (b): AIA images taken during the flare impulsive phase. A diffused coherent structure (marked "Hot channel FR") is visible in AIA 131 Å, which we refer to as an FR. A different image of AIA 193 Å shows the morphology of the envelope structure above the AR. The contours of the coaligned LOS magnetic field, ±90 G (red/blue), are overplotted in order to locate the magnetic origins of the erupting structure. Panels (c)–(e): white-light observations of the CME from LASCO C2/C3 showing the distinct leading edge, cavity, and core parts. The core is less contrasted as the CME expands further in the C3 FOV.

located nearby, in the opposite polarities on both sides of the main PIL. The onset of the eruption is accompanied by two flare ribbons and flare loops in the AIA 171 and 304 Å images, as displayed in the top row of Figure 2.

Since the erupting structure is diffused, we studied the time-difference images from AIA 131 Å to enhance the contrast with the background. Examples of the time-difference images are displayed in the bottom panels of Figure 2 (see also the accompanying animation). In these images, the ascending loops and the underlying flare loops are clearly visible. L1 and L2 are seen distinctly until 22:55 UT. In the later evolution, these loops merge as a single structure without a connection to the inner bipolar region. This implies a coronal reconnection of the loops L1 and L2, which are then transformed into flare loops and a single larger structure above. We refer to this erupting structure as a hot-channel FR (HFR), with more justifying evidence below. The HFR ascends further and eventually erupts at around 23:00 UT (more details are given in Section 3.3).

At around 23:00 UT, the AIA 304 Å images present two J-shaped flare ribbons, with the approximately straight parts being close to the PIL (Figure 2(c)). Taken together, the ribbons define a global S shape, which indicates that the HFR

has a positive twist. The straight parts of the ribbons are linked with flare loops underneath the rising HFR, and they become prominent as flare reconnection progresses. The hook parts of the ribbons surround the footpoints of the HFR, as shown by topological analysis of previous FR configurations (e.g., Démoulin et al. 1996b; Titov 2007; Savcheva et al. 2012). Said differently, the curved parts of the ribbons provide the border of the FR footpoints.

As the reconnection proceeds, the FR grows in magnetic flux, and the ribbons separate into a broader J shape. These ribbons are expected to be present at the base of the quasi-separatrix layers, which are regions where the field line connectivity changes drastically, where the current layers are formed, and where magnetic reconnection occurs (Démoulin et al. 1996a; Aulanier et al. 2010; Vemareddy & Wiegelmann 2014; Zhao et al. 2016; Vemareddy 2021). Then, the emissions, observed in 131 Å and moving away from the AR, are interpreted as the new reconnected field lines that are wrapped around the erupting FR. Furthermore, the northern hook is the most clearly observed element throughout the event. For more than one hour before any eruption signs, plasma motions were already present all along this hook (see the attached animation in 131 Å). This implies that the FR was
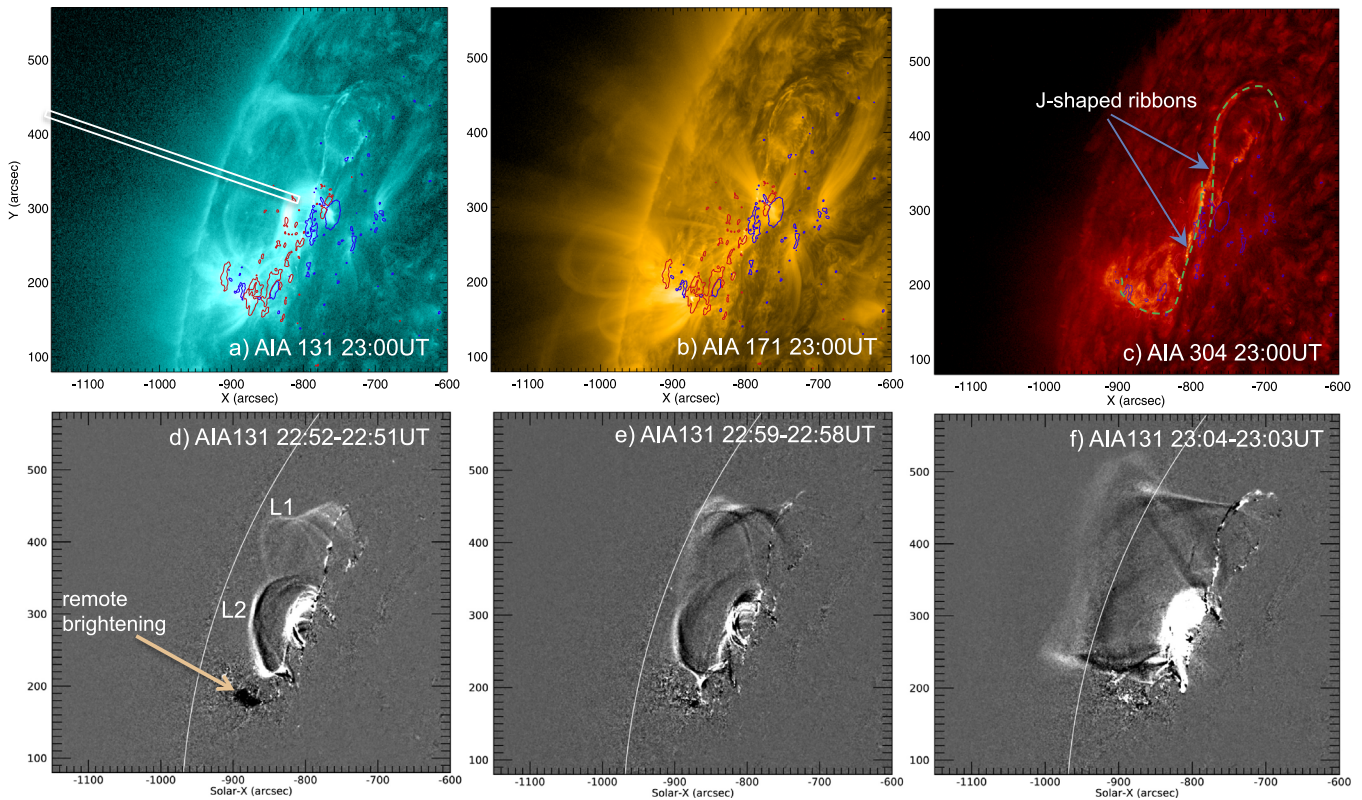
Figure 2. The onset of the eruption from AR 12282. Panels (a)–(c): images of the erupting region in the AIA 131, 171, and 304 Å channels. J-shaped ribbons are observed in AIA 304 Å from 22:55 UT onward. The contours ±90 G (red/blue) of the LOS magnetic field are also overlaid. For kinematic analysis, the slit position is shown in panel (a). Panels (d)–(f): different images of AIA 131 Å during the onset of the eruption. Two nearby loop structures, L1 and L2, first rise up, then reconnect at a coronal cross-point to form a single larger loop structure with flare loops below. A remote brightening location is marked with an arrow. The white curve outlines the edge of the limb. This scenario of the onset of the eruption is better comprehended with the online animation accompanying this figure. It has been prepared using the sequence of AIA 131 Å images (left panel) and the running difference images of AIA 131 Å (right panel). The animation start (end) time is 22:30 (23:18) UT. (An animation of this figure is available.)

already present well before the eruption, and that weak reconnection was already active, heating up and displacing the plasma at the FR boarder. We conclude that the EUV observations of the hot-channel structure together with the J-shaped flare ribbons provide evidence of the magnetic FR before and during the course of the eruption. To our knowledge, such observations of the hot channel with a clear link to the hook-shaped flare ribbon have not been shown previously.

For a clearer picture of the onset of the eruption, we have prepared a spacetime map of a slit placed across the hot channel, as shown in Figure 2(a). The map is displayed in Figure 3(a). It is clear that the rising motion starts at 22:42 UT; at this time, however, one loop (L2) intersects the slit. As the rising motion progresses, several continuous loops form, as delineated in the images after 22:55 UT. Around 23:00 UT, the two loops reconnect to form a single loop structure, and then a rapid rise is evident from then onward.

In Figure 3(b), we plot the height–time observations of the hot-channel trace. Being at 60° longitude, the derived height–time data is corrected to compensate for projection effects by assuming a radial motion. We then fit this height–time data with a linear-cum-exponential model:

$$h(t) = C_0 + C_1 t + C_2 e^{t/\tau}, \qquad (1)$$

where C_0, C_1, C_2, and τ are the four free parameters of the fit (Cheng et al. 2013). This model accommodates the slow and

rapid rising motions, so fits very well to the data points (the blue curve in Figure 3(b)). The growth time is $\tau = 24.87$ minutes. This model fit allows us to determine the transition time between the slow (nearly constant velocity) and exponential growth stages. We estimate the critical time $T_c = \tau \ln(C_1 \tau / C_2)$ at which the exponential component of the velocity equals the linear component. This is found to be February 9 at 22:55 UT, which corresponds to a height of 1.126 $R_\odot$ (87 Mm). After this time, the exponential term in Equation (1) dominates, and this behavior characterizes an instability. Note that, at this time, the rising motion also coincides with the disappearance of two loops into the continuous loop structure, which is regarded as the FR. However, the soft X-ray flux shows indications of the flare only after 23:00 UT. This means that a decreasing overlying field might also have played a role in the onset of the eventual eruption, with the flare reconnection later adding to the acceleration of the FR.

3.2. Initiation of the Eruption: Mechanism

The observations of the eruption are plausibly compatible with the model of tether-cutting reconnection formulated by Moore & Labonte (1980) and Moore et al. (2001). In this model, the AR consists of an inner bipolar region with an initial sheared magnetic arcade. When subject to a converging motion
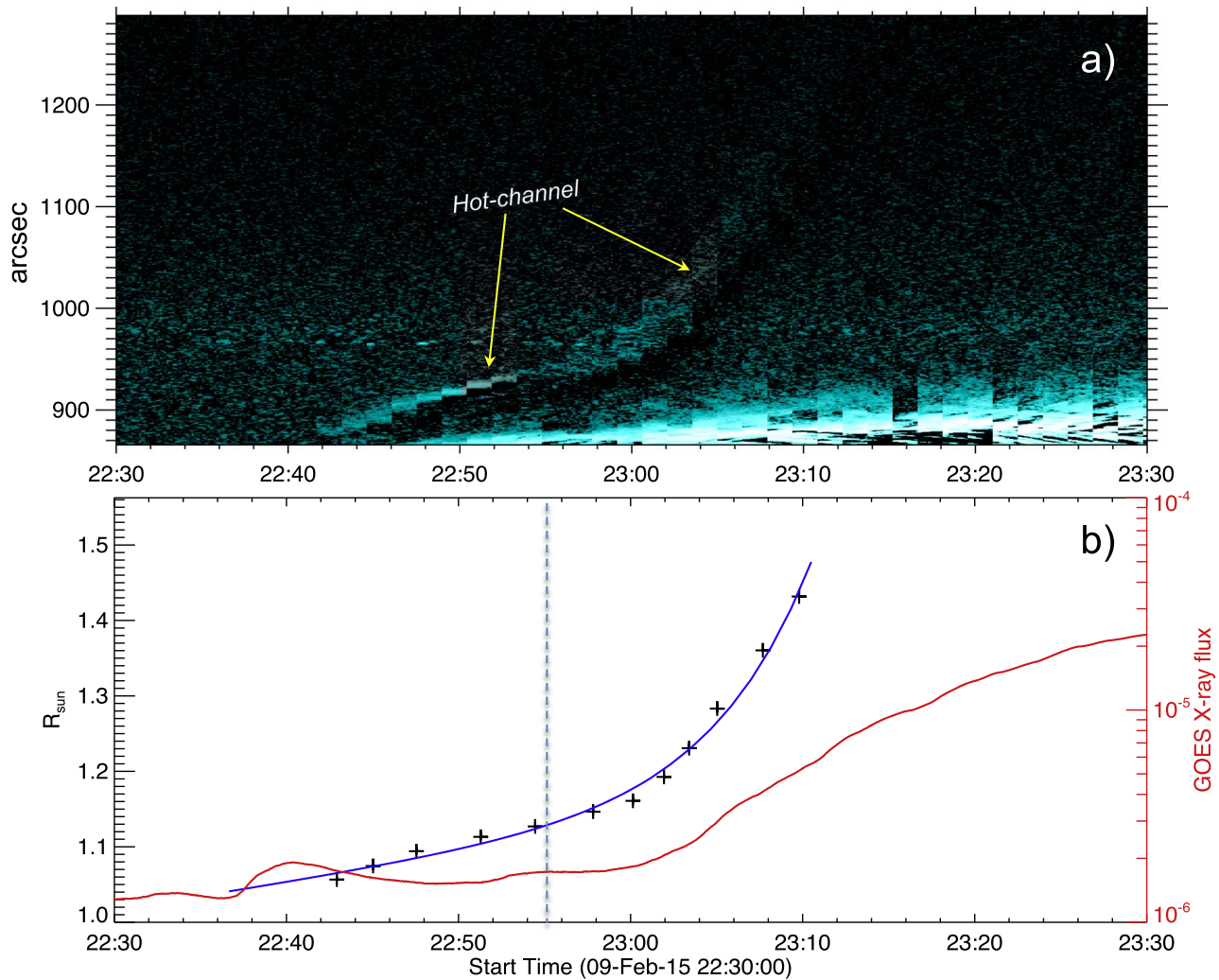
4

Figure 3. The upward-rising motion of the hot channel with time. Top: a spacetime map prepared from the slit as shown in Figure 2(a). The trace of the hot channel is indicated with the arrows. Bottom: the height–time plot of the hot channel derived from the spacetime map. Note that the height is corrected for projection effects, such that the motion is radially outward. The data points along the hot-channel trace are fitted with a linear-cum-exponential function (the blue curve), while the blue vertical dashed line marks the time at which the linear velocity is dominated by the exponential growth of the velocity, and is referred to as the critical time for the eruption's onset. The corresponding height is referred to as the critical height, which in this case is 0.126 $R_{\odot}$ (87 Mm). The GOES X-ray flux is also shown with the red curve, with the y-axis scale on the right-hand side. Noticeably, the eventual eruption accompanied by the flare occurs at 23:00 UT.

toward the PIL, the reconnection of the adjacent opposite sheared arcade loops forms an upward-rising twisted FR, as proposed by van Ballegooijen & Martens (1989). In Figure 4, we deploy this scenario of reconnection in the context of our observations. In the left-hand panel, on top of the HMI magnetogram, we add schematically the magnetic connectivities of the rising loops L1 (blue) and L2 (orange), as seen in the AIA 131 Å images (Earth view). For a clearer picture, we also display these loops on the HMI synoptic magnetogram, as if seen from above. These loops appear as two lobes of a sigmoid, as observed in other events (e.g., Vemareddy & Demóulin 2018), coherent with the observed J-shaped ribbons. This configuration is typically the precursor structure of a CME eruption.

The footpoint locations of the L1 and L2 loops show that they are in a highly sheared magnetic configuration above the PIL. After the tether-cutting reconnection of L1 and L2, the formed hot channel (FR in the models) rises due to self- or hoop force. In a successful eruption, like this one, at some point of the evolution the FR becomes unstable. This is traced by the exponential behavior of the upward velocity. Moreover, further

reconnection adds more flux to strengthen the FR, such that it can further overcome the restraining force and accelerate upward (Aulanier et al. 2010; Janvier et al. 2015). In this process, the reconnection behind the erupting structure is important for further decreasing the downward tension of the overlying arcade so that positive feedback occurs on the upward motion (Welsch 2018).

The location of the present event, close to the solar limb, implies that a magnetic field extrapolation of the coronal field is delicate. We still attempted to see whether the start of the exponential behavior was reached when the critical index of the torus instability was reached (Lin & Forbes 2000; Kliem & Török 2006). The results of the potential field extrapolation, while compatible with the torus instability, are not so reliable, as they involve a magnetogram taken more than one day later, so we omit reporting them here. Moreover, the synchronization of the hot-channel dynamics with the EUV and X-ray fluxes (Figure 3) instead points to a driving mechanism of runaway tether-cutting reconnection with positive feedback between the upward FR motion and the reconnection rate below it (Moore et al. 2001; Jiang et al. 2021).
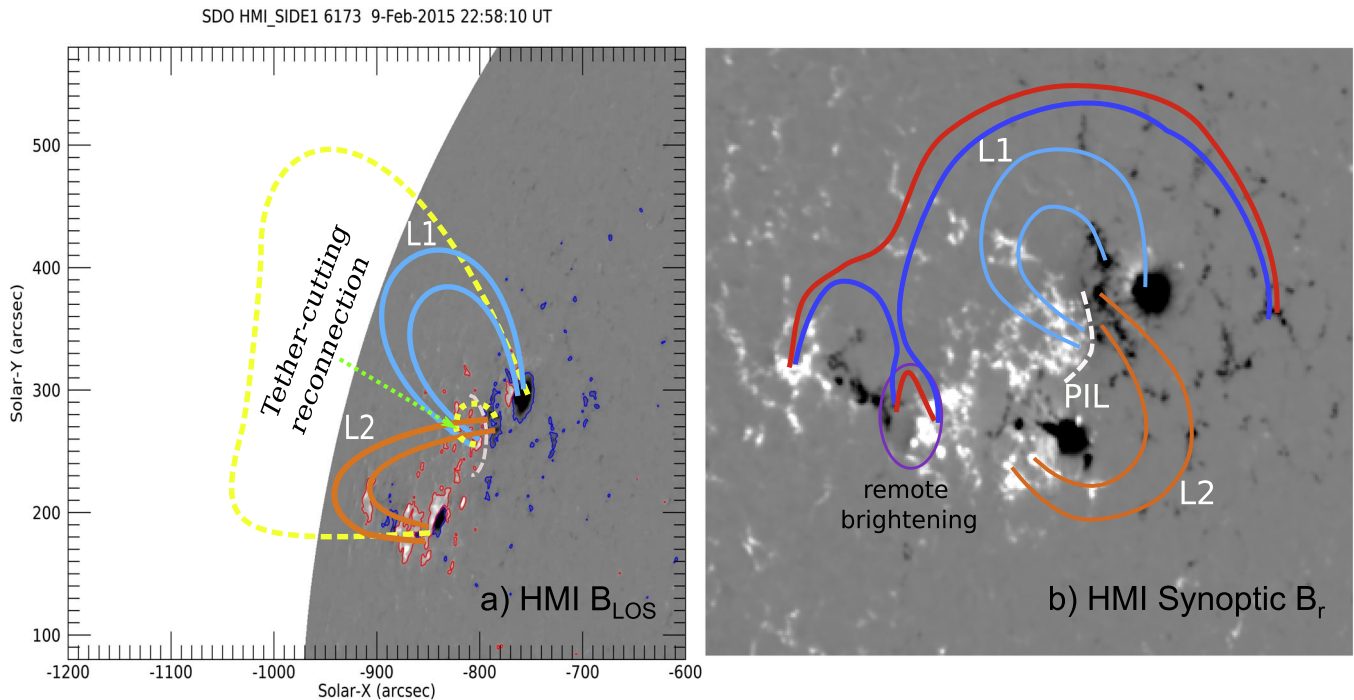
Figure 4. A schematic illustration of the possible magnetic structure undergoing the tether-cutting reconnection. Panel (a): an HMI LOS magnetogram displaying the distribution of the magnetic field. The contours of ±90 G are overlaid. The loop systems L1 (cyan) and L2 (orange) are sketched to reveal their magnetic origins. The white dashed curve is the PIL. The dashed yellow curves refer to the reconnection by-product of the loop systems L1 and L2. Panel (b): the HMI synoptic radial field distribution on February 11 at 12:00 UT. The map is the result of cylindrical equal-area projection onto the disk center. The white dashed curve refers to the PIL, with a possible sheared arcade all along. The loop systems L1 (cyan) and L2 (orange) are sketched as if they were seen from above (the dashed yellow curves for the reconnection by-product are not shown). In addition, the purple oval is the location of the remote brightening with converging opposite magnetic polarities. The reconnection scenario causing the remote brightening is also sketched in blue (before reconnection) and red (after reconnection).

Importantly, we notice a region of remote brightening well before the onset of the eruption, i.e., 22:30 UT, which may be the signature of the trigger of the onset of the slow rising motion (Figure 2(d)). Careful inspection of the animation reveals that the brightening is associated with the low-lying closed loop adjacent to the large-scale overlying loops. The external reconnection at this remote brightening region is suggested as initiating the rising motion of the erupting feature (HFR) by removing/reducing the overarching loops. This reconnection scenario is also sketched in Figure 4(b). The low-lying loop, drawn in red, has the morphology of a brightened loop as seen early on (see the animation). We interpret it as the product of the reconnection between the loops in the adjacent bipolar region with the large overlying loops (both drawn in blue). The motion of the small bipolar region toward the AR positive polarity would be the key, as can be noticed in on-disk observations, to inducing this reconnection that is cospatial with the remote brightening.

Finally, this event is similar to the on-disk eruptions of X-ray or EUV sigmoids, or H_α filaments, where the reconnection scenario could be ambiguous due to projection effects. In particular, the on-disk observations of sigmoid events studied by Vemareddy & Zhang (2014) have comparable features to this limb event. Owing to the cool background temperature, the sigmoid contrast from the background plasma emission was very good in the hot EUV channels, which is not the case here. Observational evidence for tether-cutting reconnection has also been found by employing multitudehigh-resolution imaging data (Vemareddy et al. 2017; Chen et al. 2018).

3.3. CME Kinematics

In order to derive quantitative information on the mechanisms involved in the eruption, we quantify below the kinematics of the LE and the FR. In particular, the temporal behaviors of their velocity and acceleration provide information about the net force that accelerates the plasma.

The kinematics of this event have been studied by manually tracking the CME LE and core in the LASCO/C2 and C3 FOVs. Time-difference images are used to enhance the contrast. In Figure 5, we plot the height–time observations of the core center (the bright part) and the leading edge of the CME observed in the LASCO white-light images. Height–time observations (Figure 3(b)) of the hot channel observed in AIA 131 Å are also included. A possible manual error of 4 pixels ($2''.4$, $48''$, $224''$) in each data set is shown.

Within the LASCO FOV, a second-order polynomial is sufficient to well fit the height–time LE of the CME, as shown in the upper panel of Figure 5 (the red and blue lines). Next, since the CME core is associated with the HFR, we fit the combined height–time data of the AIA HFR and CME core with a fifth-order polynomial in order to include the large variation in velocity. Although the fit of the height well represents the data, computing the time derivative reveals oscillatory-like behavior, a typical behavior of fits with high-order polynomials. In the early phase of the rising motion, this even implies negative velocities. This shows the limits of such an approach of incorporating all of the erupting phases within the same analytical formula, which needs a focused study. Then, as for the LE, we also perform a second-order polynomial fit of the CME core.
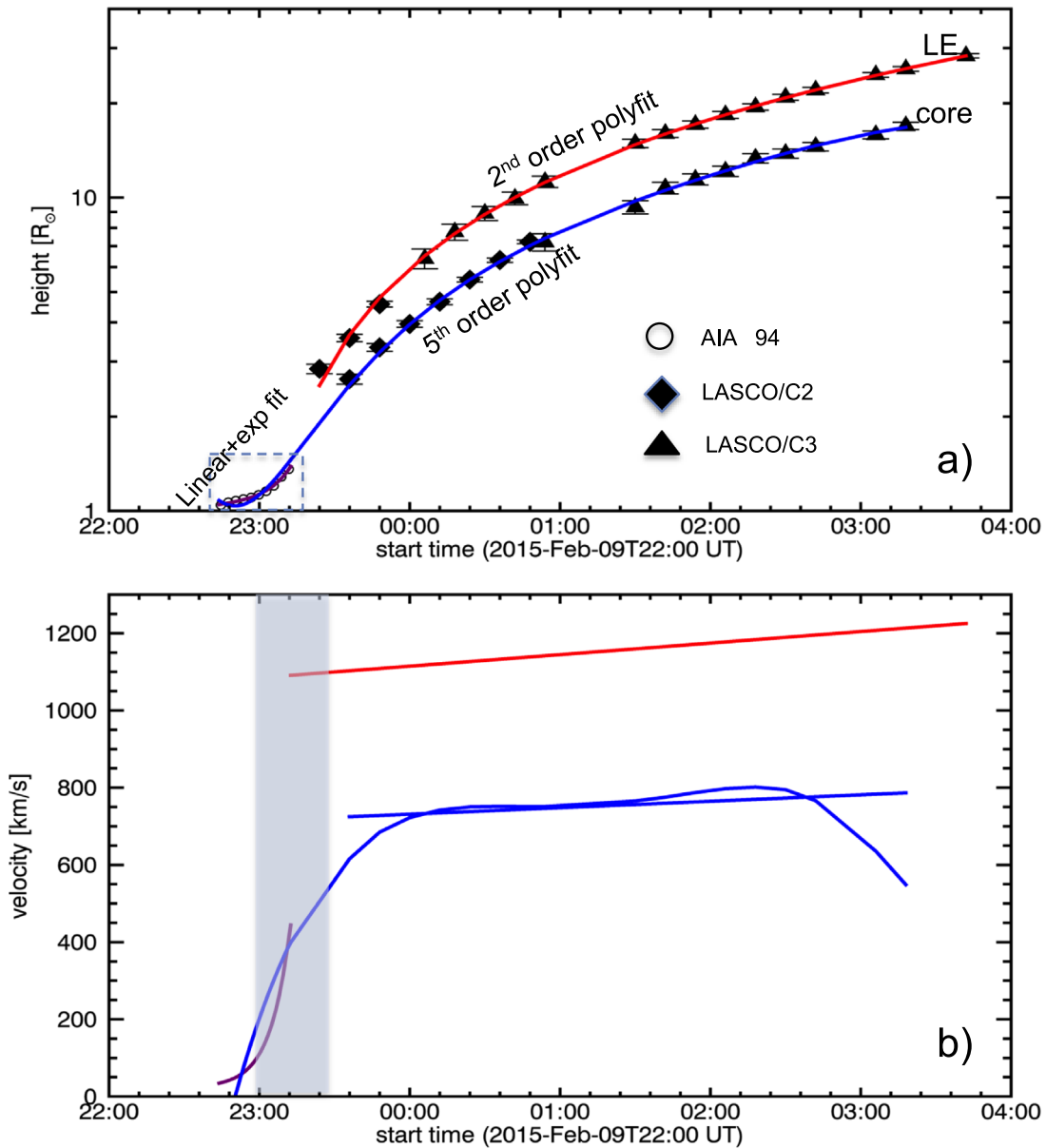
Figure 5. The kinematics of the eruption event. Panel (a): a height–time plot of the erupting HFR in the AIA FOV (the circles) and the LE and core in the LASCO FOV. The purple and red curves are the model fits to the height–time data with a linear-cum-exponential term in the AIA FOV and with a second-order polynomial model in the LASCO FOV. The blue curve is a fifth-order polynomial fit to the combined data of the HFR and CME core, which fairly represents the data except in the AIA FOV. Panel (b): the derived velocities from the model fits to the height–time data. The blue curve is from the fifth-order polynomial fit; it presents some oscillatory behavior after 00:00 UT. The purple and red curves are the linear-cum-exponential and second-order polynomial fits, respectively. The shaded region represents the rapid acceleration phase to the extent of the peak flare time February 9/23:35 UT, which is within 3 $R_\odot$. Within the AIA FOV, the velocity of the HFR rising motion increases from an initial velocity of 40–400 km s^{-1}.

From the above fitting to the data, we derive the velocity and acceleration information. Before the instability sets in, the FR rises with a nearly constant velocity of 40 km s^{-1}, which corresponds to an acceleration of 6 m s^{-2}. Thereafter, the FR runs into a rapid acceleration phase, reaching 1400 m s^{-2} in the AIA FOV. This rapid acceleration phase is well within 3 $R_\odot$, as reported earlier. In the LASCO FOV, the velocity of the LE (core) continues to increase from 1090 to 1220 (724 to 786) km s^{-1}, with a lower and steadier acceleration of about 8.3 (4.6) m s^{-2}. Therefore, in the coronagraph FOV, the CME continued to accelerate weakly, as in the case of the 2015 May 9 CME studied in Vemareddy et al. (2017). In summary, the kinematic study shows three stages of acceleration—slow, fast, and slow—which are consistent with previous studies (Zhang et al. 2001; Gopalswamy et al. 2003).

3.4. EUV Light Curves and Radio Spectra

The EUV and radio observations provide complementary information on the eruption development. Below, we complement Section 3.1 with the EUV light curves that summarize the global results of this subsection, and provide a context to interpret the radio observations. These last ones allow us to trace the various accelerations of electrons during the eruption: in the flare region, at the CME shock, and within the erupting FR, as well as those injected along open field lines in the interplanetary space.

Figure 6(c) shows the light curves of the eruption event in different wavelengths. The GOES X-ray flux is integrated over the entire disk, whereas the EUV 131, 171, 211, and 304 Å
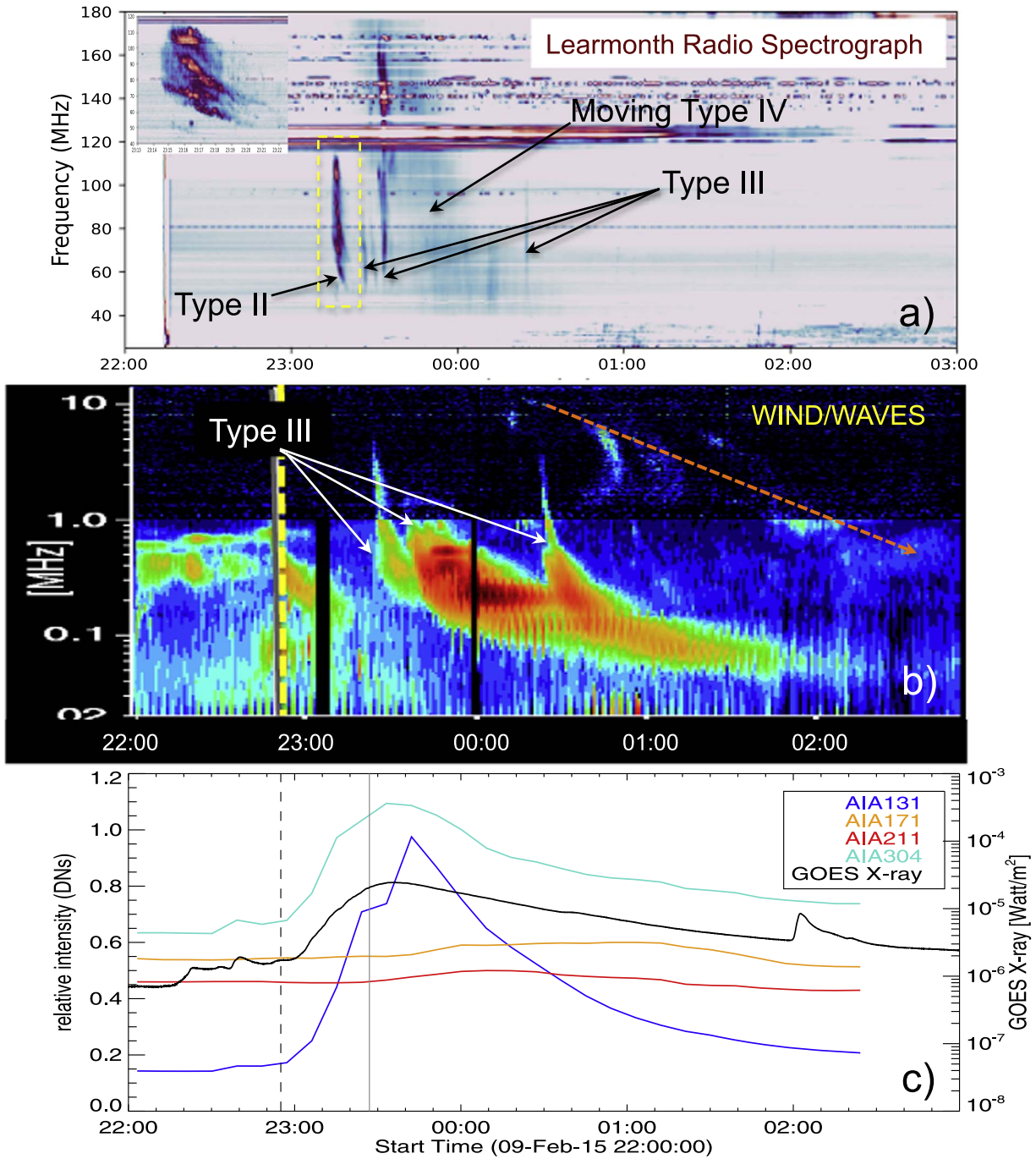
Figure 6. Radio observations and coronal emission light curves corresponding to the CME eruption. Panel (a): radio spectrum observations obtained using the Learmonth radio spectrograph. Arrows point to the type II and the moving type IV bursts triggered by the eruption. The inset plot is the zoomed-in portion of the type II burst outlined in the rectangular yellow box. Panel (b): the radio dynamic spectrum obtained with the WIND/WAVES instrument located at the Lagrange L1 point. The arrows refer to the type III bursts originating from the CME-associated flare. Panel (c): light curves of AR 12282 in EUV and X-ray wavelengths. The GOES X-ray flux is integrated over the entire disk, whereas the EUV 131, 171, 211, and 304 Å channels are integrated over the AR. The X-ray flux evolution is nearly cotemporal with the AIA 131 and 304 Å channel fluxes. The postflare emission corresponds to late-phase enhancement in the AIA 211 and 171 Å wavelengths. The dashed and solid vertical lines refer to the eruption onset (22:55 UT) and flare impulsive phase peak (23:27 UT), respectively.

channels are integrated over the AR, including the corona above the limb. The bump in AIA 304 at 22:42 UT corresponds to a soft X-ray flux, which is related to the remote brightening mentioned earlier. The flare start time is 23:00 UT, as the light curves in the EUV channels correspond well with the soft X-ray flux. The timeline of this eruption event is given in Table 1.

The preflare—or initiation—phase is associated with the rising motion of the coronal loop structures L1 and L2

(Section 3.1). The soft X-ray peak at 23:35 UT is cotemporal with the AIA 131 and 304 Å channel fluxes. This defines the M2.4 class flare. The 131 Å channel is double peaked around 5.5×10^4 and 10^7 K (Boerner et al. 2012), then it responds to the high-energy deposit similarly to soft X-rays. Also, some of the magnetic energy released by reconnection is transported toward the chromosphere, where it heats up the plasma. Indeed, the associated flare ribbons are imaged in the emission of the 304 Å channel, as this passband corresponds to chromosphere

Table 1
Timeline of the Eruption

Time (UT)	Description
22:30	Remote brightening (Figure 2(d))
22:42	Observed initiation of the rising motion (Figure 3)
22:55	Critical time of the rising motion (Figure 3)
23:00	Flare start time in the GOES X-ray flux (Figure 6(c))
23:27	The peak of the flare impulsive phase (Figure 6(c))
23:35	The flare peak time in the GOES X-ray flux (Figure 6(c))
23:14	Type II radio burst (Figure 6(a))
23:18	Type IVm radio burst (Figure 6(a))
23:27	Type III radio burst (Figure 6(b))

and transition region emissions. The emitted flux from the post-reconnection loops falls in the AIA 171 and 211 Å channels, whose response functions are peaked around 1 and 2×10^6 K, respectively. Then, their light curves are enhanced significantly much later than the flare peak time.

The dynamic radio spectrum of Figure 6(a) shows a type II burst between 23:14 UT and 23:17 UT in the frequency range 55–80 MHz (see the inset plot for a clear picture). Since it is widely accepted that the emission mechanism of type II bursts is plasma emission, with the emitting frequency scaling as the square root of the plasma density, N, the height of the emission could be estimated (Mann et al. 1995; Gopalswamy 2006, p. 207). In the present data, we do not have access to the plasma density, so we use a Newkirk density model adapted to ARs (Newkirk 1961). The estimated height range corresponding to those frequencies is ≈1.45–1.63 $R_\odot$. This height range is comparable with the height of the CME's leading edge (<2 $R_\odot$) during the same time period (Figure 5(a)). Moreover, the shock is probably located at the leading edge of the CME seen in LASCO C2 and C3 (Figure 1). Furthermore, since the source region of this event is an AR located near the limb, it is expected that only the harmonic component is to be observed in the dynamic spectrogram, with the fundamental emission not reaching Earth because of its higher directivity (Thejappa et al. 2007; Bonnin et al. 2008; Thejappa et al. 2012; Ramesh et al. 2012; Sasikumar Raja & Ramesh 2013).

Although we do not have the calibrated flux densities, to compensate for the gain variation across different frequency channels we have subtracted the median of the time series separately for all channels and measured the spectral index (α) using

$$\alpha = \frac{\ln(S_1) - \ln(S_2)}{\ln(f_1) - \ln(f_2)}, \quad (2)$$

where the $S_1 = 29$ and $S_2 = 13$ counts are the measured amplitudes of type II at the given frequencies $f_1 = 92$ MHz and $f_2 = 71$ MHz, respectively. As such, the measured spectral index of a type II burst is ≈3.

The observed drift of frequency is due to the decrease in plasma density with height. We compute this drift in the time ranges $t_1 = 23:14$ and $t_2 = 23:17$ UT. The corresponding emission frequencies of the type II are $f_1 = 80$ and $f_2 = 55$ MHz. The observed drift rate is $\Delta f/\Delta t$, where $\Delta f = f_1 - f_2$ and $\Delta t = t_2 - t_1$. The estimated drift rate is ≈0.14 MHz s^{-1}. Then, we estimate the average type II speed using the relation $v_{typeII} = \frac{2L}{f} \frac{\Delta f}{\Delta t}$, where $L = \left(\frac{1}{N}\frac{dN}{dR}\right)^{-1}$ is the plasma density scale height (≈2.31×10^5 km) and f is the averaged frequency

(Gopalswamy 2011; Mann & Klassen 2005). The estimated type II speed is ≈962 km s^{-1}, which is compatible with the mean speed of the CME's leading edge during 23:14–23:21 UT of about 1100 km s^{-1} (see Figure 5(b)).

Type III bursts are present in the dynamic radio spectrum of Figure 6(b) in the frequency range 20 KHz–14 MHz, with the meter-wave counterparts (110 MHz and below) in Figure 6(a). The type III burst in this case is cotemporal with the X-ray and EUV emissions commencing at the peak flare time (23:27 UT) defined by the time derivative of the soft X-ray flux. However, it is worth mentioning that all of the three indicated type III bursts originate after the type II burst is seen, and hence they are presumably associated with the post-eruption open magnetic loops. These emissions correspond to electrons accelerated to a fraction of light speed along open magnetic field lines (Ginzburg & Zhelezniakov 1958; Zheleznyakov & Zaitsev 1970; Melrose 1980; Sasikumar Raja & Ramesh 2013; Reid & Ratcliffe 2014; Mahender et al. 2020). They could come from the reconnection of the erupting field configuration with the surrounding open field or from the flare reconnection providing a channel to open field lines (e.g., Masson et al. 2019).

The dynamic spectrum also detected a moving type IV (type IVm) burst starting at 23:18 UT, which lasted until 00:34 UT on 2015 February 10 (Figure 6(a)). A type IVm burst is a broadband continuum emission with a clear frequency drift with time. This type IVm was observed by the Learmonth observatory, Australia, as well as the HIRAS spectrometer, Japan.[6] In both of the dynamic spectra, the type IV is observed in the frequency range 44–438 MHz. The estimated drift rate is ≈0.09 MHz s^{-1}. This indicates that the source location moves as the CME propagates radially outward (McLean & Labrum 1985; Gergely 1986). The height–time data shown in Figure 5(a) indicate that at the start time of the type IVm burst (23:18 UT), the LE (core) of the CME was located at a height of 2.1 (1.5) $R_\odot$. Similarly, at the end time (00:34 UT) of the type IVm burst, it was at 9.4 (6.1) $R_\odot$. Type IVm bursts were previously associated with the CME's core (Sasikumar Raja et al. 2014; Vasanth et al. 2019). Although we do not have imaging observations on this day, the present event could be interpreted in this general framework.

Emission mechanisms of type IV bursts are still debated, and different authors have suggested plasma emission or gyrosynchrotron or electron–cyclotron maser emission as the main emission mechanism (e.g., Sasikumar Raja et al. 2014; Vasanth et al. 2016; Carley et al. 2017). Therefore, in order to investigate the emission mechanism of this particular event, we have measured the spectral index (Equation (2)). We use $f_1 = 60$ and $f_2 = 175$ MHz, which correspond to $S_1 = 7$ and $S_2 = 5$ counts, respectively. We deduce a spectral index of ≈−0.31, suggesting that this type IVm has a gyrosynchrotron emission mechanism (Sasikumar Raja et al. 2014). More precisely, the negative sign of the spectral index is characteristic of a nonthermal emission mechanism. The small value of the spectral index indicates an optically thin gyrosynchrotron emission. Furthermore, if the emission mechanism is due to the plasma emission, the spectral index shall be $<–3$ (Melrose 1975; Sasikumar Raja et al. 2014). Since the type IVm burst does not have a plasma emission origin, however, we are unable to estimate its velocity. Finally, it is worth pointing out

---

that in WIND/WAVES, both the type II and type IVm bursts are not seen, which may be due to the sensitivity of the instrument and/or the electron energy dropping down and no being longer sufficient to generate radio emission. However, the fragmentation that is seen along the red dotted line in Figure 6(b) is presumably caused by the decahectometric and kilometric type II bursts.

4. Summary and Discussion

We analyzed a unique eruption of a hot plasma channel from its early evolution within the core of an AR. This eruption leads to a well-observed CME from the source AR 12282 near the eastern solar limb. The ejected plasma is visible mainly within the EUV hot channel of AIA 131 Å. An EUV brightening was first observed in the trailing part of the AR, with a converging motion of opposite polarities. This brightening is consistent with a middle increase in the soft X-ray flux starting at 22:30 UT. At the beginning of the eruption (22:42 UT), two highly sheared loops are visible in EUV above the main AR PIL. The two loops have two of their footpoints near each other on either side of the PIL. These two loops expand, then reconnect to form a single structure, an ejected hot structure, identified as an FR, and compact flare loops underneath.

This eruption event is similar to the one described in the tether-cutting reconnection model (Moore et al. 2001), which is responsible for the FR formation and its slow rising motion. This event has comparable observational signatures to the ones expected in numerical simulations, where a sheared arcade is forced to reconnect by the converging motions at the PIL (Aulanier et al. 2010; Zuccarello et al. 2014). Recent numerical simulations argue that the tether-cutting reconnection has a fundamental importance in the initiation of solar eruptions in a very simple bipolar active region (Jiang et al. 2021). The observed flare ribbons are J-shaped, which is an indication that the hot channel is an FR. This event is a unique event in which the flare ribbons are very clearly observed together with the erupting hot channel, which strongly suggests that the hooked parts of the J-shaped flare ribbons outline the boundary of the erupting FR.

The kinematic study reveals a three-phase evolution of the CME eruption as typically observed (e.g., Zhang et al. 2001). In the initiation phase, the FR slowly rises at a nearly constant speed of 40 km s^{-1}. This is followed by the flare impulsive phase from 23:00 UT, where a large acceleration is present to a maximum of 1400 m s^{-2} within the AIA FOV. This phase includes the exponential rising motion of the FR, which characterizes the development of an instability. Finally, the acceleration decreases in the propagation phase within the LASCO FOV. Within the C3 FOV, the CME LE (core) continues to propagate at a steady acceleration of about 8 (4) m s^{-2}.

Since the flare impulsive phase (from 23:00 UT to 23:35 UT) observed in EUV synchronizes with the rapid acceleration of the erupting FR, the flare reconnection played a major role in the outward acceleration process within 3 $R_\odot$, similar to earlier studies (Song et al. 2013; Vršnak 2016). This positive feedback from the reconnection on the acceleration is due to the further buildup of the FR, where stabilizing overlying arcades are transformed into the external layer of the erupting FR (Welsch 2018).

The CME eruption launched radio bursts of type II, III, and IVm, as observed by both ground- and space-based instruments. The type III bursts are identified with the emission drifting in the 50 KHz–180 MHz range synchronous with the flare peak time for the strongest bursts. The average type II speed is in agreement with the speed of the leading edge of the CME. The type II burst is followed by a type IVm, typically interpreted by radio emission within the core of the CME (Vasanth et al. 2016, 2019), which in this case is also the identified hot-channel FR. The start and stop times of the type IVm correspond to the CME's core height of 1.5 and 6.1 $R_\odot$, respectively. Also, the spectral index is negative, suggesting that nonthermal electrons are trapped in the closed loop structure. This event adds to the previous reports that type IVm bursts are associated with the CME's core being the hot-channel FR (Vasanth et al. 2016, 2019). However, this study lacks radio imaging observations to reveal more information about the links between the type IVm burst and the erupting CME structure at the source.

Triggering and acceleration mechanisms are key points for the propagation of CMEs in the outer corona and then in the heliosphere. For example, Zhang et al. (2001) have suggested that the final velocity of a CME is dependent on the acceleration magnitude as well as the acceleration duration, both of which can vary significantly from event to event. Continuous observations from the precursor features, especially near the limb, to the acceleration and propagation phases, up to the CME stage in white light, are key observations for better constraining our understanding of these large ejections of plasma and magnetic field. We anticipate having such observations from the Visible Emission Line Coronagraph (VELC; Raghavendra Prasad et al. 2017) on board the upcoming Aditya L1 mission. VELC and meter-wavelength radio observations probe the same heliocentric distances. Such simultaneous observations will provide more insights into eruptions and their association with solar radio bursts, specifically type II and type IVm bursts.

ORCID iDs

P. Vemareddy ⓘ https://orcid.org/0000-0003-4433-8823
P. Démoulin ⓘ https://orcid.org/0000-0001-8215-6532
K. Sasikumar Raja ⓘ https://orcid.org/0000-0002-1192-1804
J. Zhang ⓘ https://orcid.org/0000-0003-0951-2486
N. Gopalswamy ⓘ https://orcid.org/0000-0001-5894-9954
N. Vasantharaju ⓘ https://orcid.org/0000-0003-2336-5208

References

Antiochos, S. K., DeVore, C. R., & Klimchuk, J. A. 1999, ApJ, 510, 485
Aulanier, G., Török, T., Démoulin, P., & DeLuca, E. E. 2010, ApJ, 708, 314
Boerner, P., Edwards, C., Lemen, J., et al. 2012, SoPh, 275, 41
Bonnin, X., Hoang, S., & Maksimovic, M. 2008, A&A, 489, 419
Bougeret, J. L., Kaiser, M. L., Kellogg, P. J., et al. 1995, SSRv, 71, 231
Brueckner, G. E., Howard, R. A., Koomen, M. J., et al. 1995, SoPh, 162, 357
Carley, E. P., Vilmer, N., Simões, P. J. A., & Ó Fearraigh, B. 2017, A&A, 608, A137
Chen, H., Duan, Y., Yang, J., et al. 2018, ApJ, 869, 78
Chen, H., Zhang, J., Li, L., & Ma, S. 2016, ApJL, 818, L27

Cheng, X., Zhang, J., Ding, M. D., et al. 2013, ApJL, 769, L25
Cho, K. S., Gopalswamy, N., Kwon, R. Y., Kim, R. S., & Yashiro, S. 2013, ApJ, 765, 148
Démoulin, P., Henoux, J. C., Priest, E. R., & Mandrini, C. H. 1996a, A&A, 308, 643
Démoulin, P., Priest, E. R., & Lonie, D. P. 1996b, JGR, 101, 7631
Démoulin, P., Vourlidas, A., Pick, M., & Bouteille, A. 2012, ApJ, 750, 147
Forbes, T. G., & Isenberg, P. A. 1991, ApJ, 373, 294
Forbes, T. G., Linker, J. A., Chen, J., et al. 2006, SSRv, 123, 251
Gergely, T. E. 1986, SoPh, 104, 175
Gibson, S. E., Fan, Y., Török, T., & Kliem, B. 2006, SSRv, 124, 131
Ginzburg, V. L., & Zhelezniakov, V. V. 1958, SvA, 2, 653
Gopalswamy, N. 2006, in Solar Eruptions and Energetic Particles, ed. N. Gopalswamy, R. Mewaldt, & J. Torsti, Vol. 165 (Washington DC: American Geophysical Union), 207
Gopalswamy, N. 2011, in Planetary, Solar and Heliospheric Radio Emissions (PRE VII), ed. H. O. Rucker, W. S. Kurth, P. Louarn et al. (Vienna: Austrian Academy of Sciences Press), 325
Gopalswamy, N., Shimojo, M., Lu, W., et al. 2003, ApJ, 586, 562
Green, L. M., Kliem, B., & Wallace, A. J. 2011, A&A, 526, A2
Handy, B. N., Acton, L. W., Kankelborg, C. C., et al. 1999, SoPh, 187, 229
Howard, T. A., DeForest, C. E., Schneck, U. G., & Alden, C. R. 2017, ApJ, 834, 86
Illing, R. M. E., & Hundhausen, A. J. 1985, JGR, 90, 275
Janvier, M., Aulanier, G., & Démoulin, P. 2015, SoPh, 290, 3425
Jiang, C., Feng, X., Liu, R., et al. 2021, NatAs, 5, 1126
Joshi, N. C., Sterling, A. C., Moore, R. L., & Joshi, B. 2020, ApJ, 901, 38
Kliem, B., & Török, T. 2006, PhRvL, 96, 255002
Leblanc, Y., Dulk, G. A., Cairns, I. H., & Bougeret, J. L. 2000, JGR, 105, 18215
Lemen, J. R., Title, A. M., Akin, D. J., et al. 2012, SoPh, 275, 17
Lin, J., & Forbes, T. G. 2000, JGR, 105, 2375
Liu, R., Kliem, B., Török, T., et al. 2012, ApJ, 756, 59
Liu, R., Liu, C., Wang, S., Deng, N., & Wang, H. 2010, ApJL, 725, L84
Lobzin, V. V., Cairns, I. H., Robinson, P. A., et al. 2010, ApJL, 710, L58
Mahender, A., Sasikumar Raja, K., Ramesh, R., et al. 2020, SoPh, 295, 153
Mann, G., Classen, T., & Aurass, H. 1995, A&A, 295, 775
Mann, G., & Klassen, A. 2005, A&A, 441, 319
Masson, S., Antiochos, S. K., & DeVore, C. R. 2019, ApJ, 884, 143
McLean, D. J., & Labrum, N. R. 1985, Solar radiophysics : studies of emission from the sun at metre wavelengths (New York: Cambridge Univ. Press)
Melrose, D. B. 1975, SoPh, 43, 211
Melrose, D. B. 1980, SSRv, 26, 3
Moore, R. L., & Labonte, B. J. 1980, in IAU Symp. 91, Solar and Interplanetary Dynamics, ed. M. Dryer & E. Tandberg-Hanssen (Dordrecht: D. Reidel), 207
Moore, R. L., & Sterling, A. C. 2006, GMS, 165, 43
Moore, R. L., Sterling, A. C., Hudson, H. S., & Lemen, J. R. 2001, ApJ, 552, 833
Ndacyayisenga, T., Uwamahoro, J., Sasikumar Raja, K., & Monstein, C. 2021, AdSpR, 67, 1425

Nelson, G. J., & Melrose, D. B. 1985, in Solar Radiophysics: Studies of emission from the sun at metre wavelengths, ed. D. J. McLean & N. R. Labrum (New York: Cambridge Univ. Press), 333
Newkirk, G. J. 1961, ApJ, 133, 983
Nindos, A., Aurass, H., Klein, K. L., & Trottet, G. 2008, SoPh, 253, 3
Payne-Scott, R., Yabsley, D. E., & Bolton, J. G. 1947, Natur, 160, 256
Pesnell, W. D., Thompson, B. J., & Chamberlin, P. C. 2012, SoPh, 275, 3
Pontin, D. I. 2012, RSPTA, 370, 3169
Priest, E., & Forbes, T. 2000, Magnetic Reconnection: MHD Theory and Applications (Cambridge: Cambridge Univ. Press)
Raghavendra Prasad, B., Banerjee, D., Singh, J., et al. 2017, CSci, 113, 613
Ramesh, R., Lakshmi, M. A., Kathiravan, C., Gopalswamy, N., & Umapathy, S. 2012, ApJ, 752, 107
Reid, H. A. S., & Ratcliffe, H. 2014, RAA, 14, 773
Sasikumar Raja, K., & Ramesh, R. 2013, ApJ, 775, 38
Sasikumar Raja, K., Ramesh, R., Hariharan, K., Kathiravan, C., & Wang, T. J. 2014, ApJ, 796, 56
Savcheva, A., Pariat, E., van Ballegooijen, A., Aulanier, G., & DeLuca, E. 2012, ApJ, 750, 15
Schou, J., Scherrer, P. H., Bush, R. I., et al. 2012, SoPh, 275, 229
Singh, D., Sasikumar Raja, K., Subramanian, P., Ramesh, R., & Monstein, C. 2019, SoPh, 294, 112
Song, H. Q., Chen, Y., Ye, D. D., et al. 2013, ApJ, 773, 129
Stewart, R. T., Dulk, G. A., Sheridan, K. V., et al. 1982, A&A, 116, 217
Thejappa, G., MacDowall, R. J., & Bergamo, M. 2012, ApJ, 745, 187
Thejappa, G., MacDowall, R. J., & Kaiser, M. L. 2007, ApJ, 671, 894
Titov, V. S. 2007, ApJ, 660, 863
Török, T., & Kliem, B. 2005, ApJL, 630, L97
van Ballegooijen, A. A., & Martens, P. C. H. 1989, ApJ, 343, 971
Vasanth, V., Chen, Y., Feng, S., et al. 2016, ApJL, 830, L2
Vasanth, V., Chen, Y., Lv, M., et al. 2019, ApJ, 870, 30
Vemareddy, P. 2021, FrP, 9, 605
Vemareddy, P., & Démoulin, P. 2018, ApJ, 857, 90
Vemareddy, P., Gopalswamy, N., & Ravindra, B. 2017, ApJ, 850, 38
Vemareddy, P., Maurya, R. A., & Ambastha, A. 2012, SoPh, 277, 337
Vemareddy, P., & Wiegelmann, T. 2014, ApJ, 792, 40
Vemareddy, P., & Zhang, J. 2014, ApJ, 797, 80
Vourlidas, A., Carley, E. P., & Vilmer, N. 2020, FrASS, 7, 43
Vourlidas, A., Lynch, B. J., Howard, R. A., & Li, Y. 2013, SoPh, 284, 179
Vršnak, B. 2016, AN, 337, 1002
Welsch, B. T. 2018, SoPh, 293, 113
Wu, Z., Chen, Y., Huang, G., et al. 2016, ApJL, 820, L29
Xue, Z., Yan, X., Yang, L., et al. 2017, ApJL, 840, L23
Yurchyshyn, V., Karlický, M., Hu, Q., & Wang, H. 2006, SoPh, 235, 147
Zhang, J., Cheng, X., & Ding, M.-D. 2012, NatCo, 3, 747
Zhang, J., Dere, K. P., Howard, R. A., Kundu, M. R., & White, S. M. 2001, ApJ, 559, 452
Zhao, J., Gilchrist, S. A., Aulanier, G., et al. 2016, ApJ, 823, 62
Zheleznyakov, V. V., & Zaitsev, V. V. 1970, SvA, 14, 47
Zuccarello, F. P., Seaton, D. B., Mierla, M., et al. 2014, ApJ, 785, 88